Thermoelectric performance of multiphase XNiSn (X = Ti, Zr, Hf) half-Heusler alloys

Downie, R. A.; Maclaren, D. A.; Bos, Jan-Willem G

Published in:
Journal of Materials Chemistry A

DOI:
10.1039/c3ta13955g

Publication date:
2014

Journal of Materials Chemistry A

RSC Publishing

PAPER

View Article Online
View Journal

Cite this: DOI: 10.1039/c3ta13955g

Thermoelectric performance of multiphase XNiSn (X = Ti, Zr, Hf) half-Heusler alloys†

R. A. Downie,[a] D. A. MacLaren[b] and J.-W. G. Bos*[a]

Received 1st October 2013
Accepted 5th November 2013

DOI: 10.1039/c3ta13955g

www.rsc.org/MaterialsA

Quantitative X-ray powder diffraction analysis demonstrates that mixing Ti, Zr and Hf on the ionic site in the half-Heusler structure, which is a common strategy to lower the lattice thermal conductivity in this important class of thermoelectric materials, leads to multiphase behaviour. For example, nominal $Ti_{0.5}Zr_{0.5}NiSn$ has a distribution of $Ti_{1-x}Zr_xNiSn$ compositions between $0.24 \leq x \leq 0.70$. Similar variations are observed for $Zr_{0.50}Hf_{0.5}NiSn$ and $Ti_{0.5}Hf_{0.5}NiSn$. Electron microscopy and elemental mapping demonstrate that the main compositional variations occur over micrometre length scales. The thermoelectric power factors of the mixed phase samples are improved compared to the single phase end-members (*e.g.* $S^2/\rho = 1.8$ mW m^{-1} K^{-2} for $Ti_{0.5}Zr_{0.5}NiSn$, compared to $S^2/\rho = 1.5$ mW m^{-1} K^{-2} for TiNiSn), demonstrating that the multiphase behaviour is not detrimental to electronic transport. Thermal conductivity measurements for $Ti_{0.5}Zr_{0.5}NiSn_{0.95}$ suggest that the dominant reduction comes from Ti/Zr mass and size difference phonon scattering with the multiphase behaviour a secondary effect.

Introduction

Waste heat recovery using thermoelectric generators is widely expected to become an important component of a sustainable energy future.[1–7] To achieve this, mass producible, high-performance thermoelectric materials are needed. The energy conversion efficiency of a material is given by its figure of merit, $ZT = (S^2\sigma/\kappa)T$, where S is the Seebeck coefficient, σ the electrical conductivity and κ is the sum of the lattice (κ_{lat}) and electronic (κ_{el}) thermal conductivity. The central challenge in thermoelectric research is to find materials where S, σ and κ can be decoupled so that large ZT values become possible. Materials with the half-Heusler structure are currently attracting much interest as thermoelectric materials due to their naturally large Seebeck coefficients and low electrical resistivities. Unfortunately, their performance is limited by a relatively large thermal conductivity ($\kappa \approx 4$ W m^{-1} K^{-1}). The crystal structure of these materials consists of a covalent zincblende $(YZ)^{n-}$ framework, which is filled with positive X^{n+} cations.[8,9] Semiconducting behaviour is observed for compositions with 18 valence electrons, the most studied of which are based on XNiSn (n-type) and XCoSb (p-type).[10–13] Mixtures of X cations (commonly Zr and Hf) are used to introduce mass differences, which reduce the thermal conductivity through point defect scattering. Less well understood is the use of mixtures of Ti and Zr/Hf, where significant differences in ionic radii exist. This extra degree of freedom leads to substantial local strain, which can be exploited to minimise the lattice thermal conductivity and was used to achieve $ZT = 1.5$ in samples with composition $Ti_{0.5}(Zr_{0.5}Hf_{0.5})_{0.5}NiSn$.[14] This result has remained irreproducible,[15] although promising gains in ZT have been reported recently.[16,17] The large ZT values are found for samples where κ has been reduced to 2–3 W m^{-1} K^{-1}, which is linked to the preparation method, but the microscopic cause of the reduction is not clear. There is a general dearth of information on the correlation between composition, structure and properties of the half-Heusler materials. In particular, our earlier work indicated that arc-melted $Ti_{0.5}Zr_{0.5}NiSn$ consisted of multiple half-Heusler phases.[18] This is not widely appreciated in the literature and has not been quantified, but could be relevant for the low lattice thermal conductivities observed in the $ZT = 1.5$ samples. Multiphase behaviour was recently considered as a plausible explanation for the large ZT values reported in refs. 16 and 17. The aim of the present study was to assess the impact of the multiphase behaviour on the thermoelectric properties. We previously prepared TiNiSn samples by arc-melting but found that this also produced $TiNi_2Sn$, Sn and Ti_5Sn_3, which gradually converted to TiNiSn upon prolonged annealing.[18–20] This was circumvented by using standard solid state reactions to gain maximum control over final composition and sample homogeneity. Our study includes a variety of n-type materials: stoichiometric $Ti_{1-x}Zr_xNiSn$ ($0 \leq x \leq 1$), nominally Sn deficient $Ti_{1-x}Zr_xNiSn_{0.95}$ ($0 \leq x \leq 1$), $Ti_{0.50}Hf_{0.50}NiSn$, $Zr_{0.50}Hf_{0.50}NiSn$

[a]Institute of Chemical Sciences and Centre for Energy Storage and Recovery, School of Engineering and Physical Sciences, Heriot-Watt University, Edinburgh, EH14 4AS, UK. E-mail: j.w.g.bos@hw.ac.uk

[b]SUPA, School of Physics and Astronomy, University of Glasgow, Glasgow, G12 8QQ, UK

† Electronic supplementary information (ESI) available: Laboratory X-ray powder diffraction data for all samples. Refined phase distributions and thermoelectric properties of the $Ti_{1-x}Zr_xNiSn_{0.95}$ series. Low resolution image of the $Ti_{0.5}Zr_{0.5}NiSn$ FIB lamella. See DOI: 10.1039/c3ta13955g

and HfNiSn. All samples were characterised using X-ray powder diffraction and measurement of the thermoelectric power factor. Thermal conductivity, transmission electron microscopy and energy dispersive X-ray elemental mapping data were collected for a subset of the samples.

Experimental

All samples were prepared by standard solid state reactions. Powders of the elemental precursors (Ti, 150 mesh; Zr, 325 mesh; Hf, 150 mesh; Ni, 120 mesh; Sn, 100 mesh) were mixed using a mortar and pestle, cold pressed and heated at 900 °C in vacuum sealed quartz tubes. The purities of all starting materials were >99.9%. All samples were initially heated for 1 day, homogenised using mortar and pestle, pressed into pellets and then re-heated without further homogenisation. A preliminary Sn deficient $Ti_{1-x}Zr_xNiSn_{0.95}$ series was used to establish optimal anneal time. To that end, 6 separately mixed 2 gram batches with composition $Ti_{0.5}Zr_{0.5}NiSn_{0.95}$ were heated at 900 °C for 1 day, followed by 3 days, 1, 2, 3, 4 and 6 weeks. Simultaneously, a series of $Ti_{1-x}Zr_xNiSn_{0.95}$ ($0 \leq x \leq 1$) samples were also prepared by annealing for 6 weeks (3 gram scale). This revealed that 2 weeks was sufficient as no change in the X-ray diffraction patterns was observed after this point. The Sn deficiency was initially chosen to better understand the compositional stability of these samples. However, subsequent work showed that the Sn deficiency does not survive in the final product.[18] These samples acquired a light residue, accompanied by a discolouration of the quartz tubes, which increased with annealing time. The residue was easily removed by sanding the pellets but could be completely prevented by wrapping them in Ta foil. The $Ti_{1-x}Zr_xNiSn_{1-y}Sb_y$ series ($0 \leq x \leq 1$), HfNiSn, $Zr_{0.5}Hf_{0.5}NiSn$ and $Ti_{0.5}Zr_{0.5}NiSn$ samples were therefore prepared by heating for 2 weeks at 900 °C wrapped inside Ta foil with one intermediate homogenisation at 1 day (3 gram scale). Laboratory X-ray powder diffraction patterns were collected on a Bruker D8 Advance diffractometer with monochromated Cu α_1 radiation. Datasets of 8 hours were used for Rietveld analysis. Rietveld fits were performed using the GSAS and EXPGUI suite of programs.[21,22] The temperature dependence of the Seebeck coefficient and electrical resistivity were measured between 35 and 500 °C using a Linseis LSR-3 high temperature Seebeck and resistance probe. The thermal conductivities of two Sn deficient $Ti_{0.5}Zr_{0.5}NiSn_{0.95}$ samples were measured between 50 °C and 500 °C using an Anter Flashline 3000 flash diffusion instrument. A Pyroceram reference sample was used to estimate the heat capacity. The sample densities were 79(1)% (3 days annealed sample) and 82(1) % (6 weeks annealed sample). Energy dispersive X-ray (EDX) analysis and Transmission Electron Microscopy (TEM) were undertaken on a JEOL ARM 200cF instrument operated at 200 kV and equipped with a Bruker XFlash detector. Data were acquired under the Spectrum Imaging protocols of Gatan's Digital Micrograph software package. A thin lamella was cut from a sintered pellet using the focused Ga^+ beam of an FEI Nova Dual Beam instrument, employing standard lift-out and polishing techniques. Damage to the surface region was minimised by *in situ* deposition of a thin Pt capping layer. The approximately $2.5 \times 4.5\ \mu m^2$ lamella was thinned to around 100 nm thickness, slightly too thick for high resolution transmission electron microscopy but sufficient to avoid fragmentation of the sintered grains.

Structural results

Multiphase behaviour in $Ti_{1-x}Zr_xNiSn$

The X-ray powder diffraction profile for the stoichiometric $Ti_{1-x}Zr_xNiSn$ series reveals the presence of sharp symmetric lines for the $x = 0$ and 1 end-members (Fig. S1a†). The intermediate compositions, however, exhibit significant broadening of the Bragg reflections. LeBail fits confirmed TiNiSn and ZrNiSn to be single phase, while the $x = 0.25$, 0.5 and 0.75 samples were modelled using 3–4 half-Heusler phases with different lattice parameters. This is illustrated in Fig. 1a, where the diffraction data for $Ti_{0.5}Zr_{0.5}NiSn$ has been fitted using 4 distinct $Ti_{1-x}Zr_x$-NiSn phases. Similar fits were carried out for the $x = 0.25$ and $x = 0.75$ samples. Trial Rietveld fits showed that it was not possible to accurately refine the fractional occupancy of the X-site. Instead, lattice parameters derived from LeBail fits (Table 1) were used to calculate the composition of each of the phases present using Vegard's law ($a = Px + Q$). These values were then combined with the phase fractions to yield an average value of x (Table 1) that in all cases closely matched the nominal value of x, demonstrating that the sample composition has not changed during synthesis. The half-Heusler phases all showed substantial peak broadening, which was attributed to further compositional variations. In all fits, refinement of one Gaussian (GW) and one Lorentzian (LY) parameter was sufficient to model the peak shape. Refinement of these parameters for $x = 0$ and 1 yielded almost identical values of GW $\approx 0.12°$ and LY $\approx 0.05°$. These values were taken to represent the instrumental broadening and any broadening inherent to these samples that is not attributable to mixing Ti^{4+} and Zr^{4+}. For the mixed phase samples, the GW parameter was kept fixed, while the LY parameter, which accounts for microstrain ($\Delta d/d$), was allowed to be refined freely. Using Vegard's law it is possible to relate $\Delta d/d$ to a compositional variation (Δx): $\Delta d/d = \Delta a/a \approx (P/Q)\Delta x$. The resulting values for Δx_i are given in Table 1. Each fitted phase is therefore characterised by an average composition (x_i) and a compositional spread (Δx_i). This compositional variation is schematically illustrated in the inset to Fig. 1a, which displays the abundance of each phase, along with its compositional variation. The $x = 0.50$ sample therefore has a semi-continuous distribution of $Ti_{1-x}Zr_xNiSn$ phases with approximate limits $0.24 \leq x \leq 0.70$, and spans a total $\Delta x \approx 0.5$. The $x = 0.25$ sample has limits $0.16 \leq x \leq 0.43$ ($\Delta x \approx 0.3$, Table 1). The $x = 0.75$ sample does not have a semi-continuous distribution but has approximate boundaries of $0.08 \leq x \leq 0.32$, $0.68 \leq x \leq 0.86$ and $0.94 \leq x \leq 1.0$. The preliminary Sn deficient $Ti_{1-x}Zr_xNiSn_{0.95}$ series shows analogous multiphase behaviour, albeit with somewhat narrower compositional spreads (*e.g.* $\Delta x \approx 0.3$ for $x = 0.50$). The results of the structural fits to the Sn deficient series are summarized in Table S1† and the collected X-ray powder diffraction patterns are shown in Fig. S2 (see ESI†). In previous work on arc-melted $Ti_{1-x}Zr_xNiSn_{0.95}$ we observed that interstitial

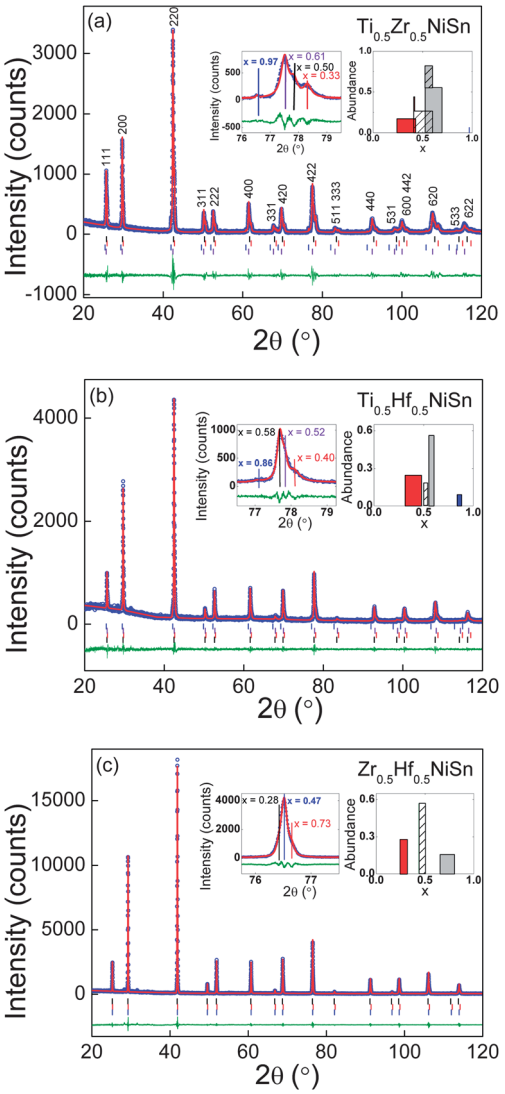

Fig. 1 Observed (blue circles), calculated (red line) and difference (green line) Lebail profiles for fits to X-ray powder diffraction data for (a) $Ti_{0.5}Zr_{0.5}NiSn$, (b) $Ti_{0.5}Hf_{0.5}NiSn$ and (c) $Zr_{0.5}Hf_{0.5}NiSn$. The Bragg reflection markers correspond to the half-Heusler phases used to obtain a satisfactory fit. The insets show a close-up of the fit to the (422) reflection, demonstrating the multiphase behaviour, and give an indication of the distribution of *x*-values in this sample. The latter histograms were obtained by combining x_i, Δx_i and the mole fractions for the phases used to fit the diffraction pattern.

Ni is present[18] and manifests itself as a shoulder in X-ray powder diffraction data. This shoulder is completely masked by the multiphase behaviour for $x \neq 0, 1$. However, a small shoulder is present for the Sn deficient $x = 0$ sample. The lattice parameters (Table S1†) may be used to estimate the amount of excess Ni,[18] which suggests that this sample contains equal ratios of TiNiSn and $TiNi_{1.02(1)}Sn$.

Multiphase behaviour in $Ti_{0.5}Hf_{0.5}NiSn$ and $Zr_{0.5}Hf_{0.5}NiSn$

Hf-doped samples were modelled and analysed in exactly the same way as the $Ti_{1-x}Zr_xNiSn$ series. The Gaussian and Lorentzian profile parameters for HfNiSn were, within error, identical to those for TiNiSn and ZrNiSn. The collected X-ray powder diffraction data are shown in Fig. S1b.† The reflections for $Ti_{0.5}Hf_{0.5}NiSn$ (Fig. 1b) are again broadened and can be modelled using 4 half-Heusler phases (Fig. 1b, Table 1). The compositional range is again semi-continuous and spans $0.32 \leq x \leq$ to 0.61 ($\Delta x \approx 0.3$), which is about 40% smaller than for $Ti_{0.5}Zr_{0.5}NiSn$. This reduction derives from both a narrower spread in x_i and smaller Δx_i values (inset to Fig. 1b). The X-ray reflections for $Zr_{0.5}Hf_{0.5}NiSn$ are much sharper but closer inspection reveals similar multiphase behaviour and 3 half-Heusler phases are needed to adequately fit the diffraction pattern (Fig. 1c, Table 1). The phase distribution is not continuous and the approximate compositional boundaries are $0.25 \leq x \leq 0.31$, $0.44 \leq x \leq 0.50$ and $0.64 \leq x \leq 0.80$ (inset to Fig 1c).

Table 1 Nominal composition, lattice parameter (a), Vegard composition (x_i), composition spread (Δx_i), molar percentage (mol%), average composition (x_{avg}) and goodness-of-fit (χ^2) for the $Ti_{1-x}Zr_xNiSn_{1-y}Sb_y$, $Zr_{1-x}Hf_xNiSn$ and $Ti_{1-x}Hf_xNiSn$ series.

x,*y*	a (Å)	x_i	Δx	mol%	x_{avg}	χ^2
$Ti_{1-x}Zr_xNiSn_{1-y}Sb_y$						
0	5.9300(1)	0	0	100	0	1.9
0.25	5.9340(1)	0.02(1)	0	1.4(7)	0.27(1)	1.9
	5.9724(1)	0.24(1)	0.17(1)	71.4(7)		
	5.9923(2)	0.35(1)	0.16(1)	27.2(7)		
0.5	5.9883(2)	0.33(1)	0.18(1)	17.3(2)	0.52(1)	2.3
	6.0189(2)	0.50(1)	0.18(1)	26.7(6)		
	6.0385(1)	0.61(1)	0.17(1)	55.4(2)		
	6.1024(3)	0.97(1)	0	6.6(6)		
0.75	5.9646(2)	0.20(1)	0.24(1)	7.9(2)	0.78(1)	2.1
	6.0662(1)	0.77(1)	0.18(1)	60.4(2)		
	6.1022(1)	0.97(1)	0.06(1)	31.7(2)		
1.0	6.1079(1)	1	0	100	1	2.1
0.5, 0.01	5.9977(2)	0.38(1)	0.26(1)	31.7(4)	0.51(1)	2.6
	6.0310(1)	0.57(1)	0.18(1)	67.2(4)		
	6.1005(3)	0.98(1)	0	1.1(1)		
0.5, 0.02	5.9972(1)	0.38(1)	0.16(1)	26.4(4)	0.51(1)	3.2
	6.0247(1)	0.53(1)	0.18(1)	67.9(4)		
	6.0998(2)	0.95(1)	0.09(1)	5.7(1)		
$Zr_{1-x}Hf_xNiSn$						
0.5	6.0849(1)	0.73(2)	0.15(1)	15.4(6)	0.45(1)	2.5
	6.0931(1)	0.47(1)	0.05(1)	56.9(6)		
	6.0992(1)	0.28(2)	0.05(1)	27.8(6)		
1	6.0764(1)	0	0	100	0	2.4
$Ti_{1-x}Hf_xNiSn$						
0.5	5.9891(2)	0.40(1)	0.16(1)	24.6(6)	0.52(1)	1.4
	6.0058(1)	0.52(1)	0.04(1)	18.1(2)		
	6.0149(1)	0.58(1)	0.05(1)	56.4(6)		
	6.0559(5)	0.86(1)	0.04(1)	0.9(1)		

EDX analysis of $Ti_{0.5}Zr_{0.5}NiSn$

A low magnification image of the FIB lamella prepared from the $Ti_{0.5}Zr_{0.5}NiSn$ pellet is shown in Fig S3.† The lamella clearly comprises several particles that have started to thin unevenly and to separate from each other during the final stages of ion polishing. Four distinct regions, typically of order 500 × 500 nm^2 in size, were analysed using EDX spectroscopy: the

approximate locations are indicated in Fig. S3.† Compositional analysis of the four regions is presented in Fig. 2, where the images in the left column are dark field scanning TEM (STEM) images with contrast dominated by thickness, mass and diffraction effects. The panels in the right column derive from a 'spectrum image' of each region, acquired by collecting EDX spectra from 10 × 10 nm^2 pixels across the area. Background-subtracted Zr–K, Sn–L, Ti–K and Ni–K EDX peaks were integrated to generate pixel-by-pixel composition maps using (standard-less) Cliff–Lorimer analysis, a protocol that is sufficient to reveal relative composition variations within the lamella but can be less reliable for absolute quantification.[23] The material in each of the four regions appears structurally different. Fig. 2a is of a particle with a generally smooth composition. The STEM contrast is modulated by brighter bands that are consistent with grain boundaries within the particle but there is no evidence of sharp features such as the spots and lines often observed elsewhere in materials with nanoinclusions.[24] Images collected at higher resolution (not shown) did not reveal any such features on shorter lengthscales. The four panels within Fig. 2b are composition maps of this first region and reveal no statistically-significant spatial variations in composition, either by direct analysis of EDX peak intensities or principle component analysis.[23] For example, there is no obvious compositional trend associated with the brighter grain boundaries of the STEM image. Indeed, histograms of pixel-by-pixel X-ray counts for the four elements do not show broadening beyond that expected for Poisson statistics. The material in image Fig. 2c, and associated maps of Fig. 2d yield a similar result; in this case, the analysis region straddles three distinct particles and aside from a small Ti-rich impurity, the three particles are largely homogeneous, do not show substantial compositional variations and have no clear regions of Ti or Zr enrichment across the 10 nm to 1000 nm lengthscales probed. The material analysed in Fig. 2e–g, on the other hand, appears less uniform. Both STEM images have noticeable black-white contrast variations that suggest that the powdered material has not fully fused and recrystallised to form uniform particles. Although the majority of features apparent in the STEM images do not correspond to pronounced changes in composition, there are complementary regions of Zr enhancement and Ti depletion in both cases, whilst narrow bands within the Sn maps suggest slight Sn segregation to grain boundaries. Compositional variations within these two areas are below 10 atomic% and it is notable that they span relatively large areas rather than discrete locations within a background matrix.

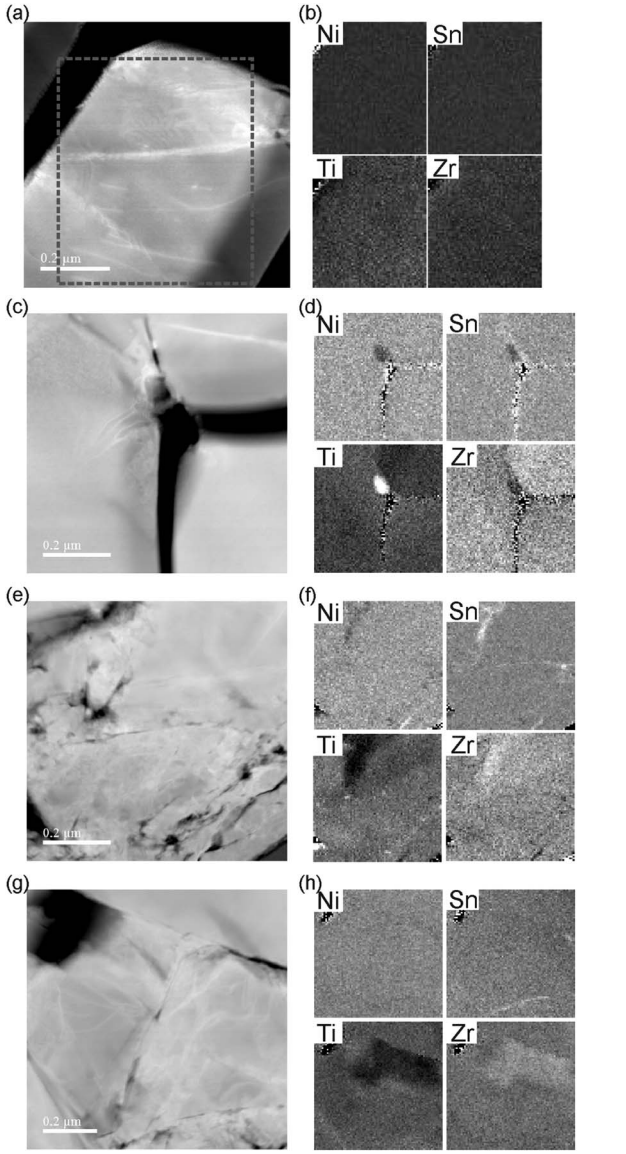

Fig. 2 Energy dispersive X-ray analysis elemental analysis of four regions within a thin lamella cut from the sintered $Ti_{0.5}Zr_{0.5}NiSn$ pellet. The images in the left-hand column (a,c,e and g) are STEM dark-field images of the four regions. The panels in the right-hand column (b,d,f and h) are associated elemental maps, showing the profiles of Ti, Zr, Ni and Sn within each analysis region, based on 10 nm × 10 nm pixels. In the first region, maps (b) derive from the dashed rectangular area of (a) whilst subsequent maps derive from the whole STEM image. The derived composition for the first area is Ti : Zr : Ni : Sn = 13% : 26% : 29% : 32%, similar to that of the other 3 regions and approximately corresponding to the composition $Ti_{0.33}Zr_{0.67}NiSn$. All four regions are therefore relatively rich in Zr and deficient in Ti.

In summary, the most significant result from the STEM-EDX analysis is the identification of particle-by-particle microstructural variations that are consistent with the large-scale multiphase behaviour and continuous compositional spread identified by XRD analysis. Some particles (such as those of Fig. 2a and c) are homogenous and of a uniform composition that may deviate from that of the complete pellet. Other particles show greater structural and compositional variations on a 100 nm length scale and are

presumably further from local thermodynamic equilibrium. In these cases there is some evidence of Sn segregation at grain boundaries and of complementary variations in Ti and Zr content. All of the particles analysed lacked the characteristic contrast variations in STEM images that would be consistent with the strain fields of small inclusions on a sub-10 nm lengthscale.

Thermoelectric properties

The temperature dependence of the electrical resistivity ($\rho = 1/\sigma$), Seebeck coefficient (S) and power factor (S^2/ρ) for $Ti_{1-x}Zr_xNiSn$ are shown in Fig. 3. All non-Sb doped samples are characterised by large, negative $S = -320$–385 μV K^{-1} at room temperature (RT), decreasing to approx. -280 μV K^{-1} at 700 K. All samples exhibit very similar behaviour and the magnitudes of $S(T)$ are in line with the best reported values.[14] All $Ti_{1-x}Zr_x$-NiSn samples are semiconductors, with $\rho = 10$–20 mΩ cm at RT and 5 mΩ cm at 700 K. The exception is ZrNiSn which has $\rho(T)$ values over 4 times higher than the rest of the samples. The densities of these samples fall between 65% of the theoretical density for the end-members to 80% for $x = 0.50$ (Table 2). As a result, the $\rho(T)$ values are approximately double those reported in the literature. Nonetheless, the large $S(T)$ means promising $S^2/\rho \approx 1.75$ mW m^{-1} K^{-2} are observed for $x = 0.25$ and 0.50 at 700 K, while the $x = 0$ sample has 1.50 mW m^{-1} K^{-2} at 700 K. The electronic properties of the promising $x = 0.5$ sample were optimised using Sb doping (Fig. 3). The introduction of additional charge carriers causes a rapid reduction of $\rho(T)$ and yields a metallic temperature dependence with values of around 1 mΩ cm at RT, rising to 2 mΩ cm at 700 K for 0.5% Sb. Further reductions in ρ are found in the samples doped with 1 and 2% Sb. The effect on $S(T)$ is a reduction over the entire measured temperature range but the drop is most pronounced at RT, where S decreases from -320 μV K^{-1} to -200 μV K^{-1} for 0.5% Sb. Further increases in doping result in further decreases in $S(T)$. The thermoelectric power factor is optimised for samples doped with 1–2% Sb and attains a maximum value of $S^2/\rho \approx 2.75$ mW m^{-1} K^{-2} at 650 K. The nominally Sn deficient samples behave very similarly (Fig. S4†). These samples are characterised by slightly lower S (-200–250 μV K^{-1} at RT, -175–225 μV K^{-1} at 700 K) and reduced ρ (4–10 mΩ cm at RT, 2–4 mΩ cm at 700 K). The lower $S(T)$ values are compensated by the reduced $\rho(T)$, resulting in similar S^2/ρ values when compared with their stoichiometric counterparts (Fig. S3†). The $Ti_{0.5}Hf_{0.5}NiSn$ sample exhibits very similar behaviour to $Ti_{0.5}Zr_{0.5}NiSn$, with almost identical values for $S(T)$ (Fig. 4). A slight increase in $\rho(T)$ leads to a reduced S^2/ρ (Table 2). $Zr_{0.5}Hf_{0.5}NiSn$ shows markedly different behaviour, with a clear maximum at ~525 K (Fig. 4). Similar behaviour is observed for HfNiSn (Fig. 4). This leads to maximum S^2/ρ values of 1.6 ($x = 0.5$) and 0.8 mW m^{-1} K^{-2} ($x = 0$) at ~620 K.

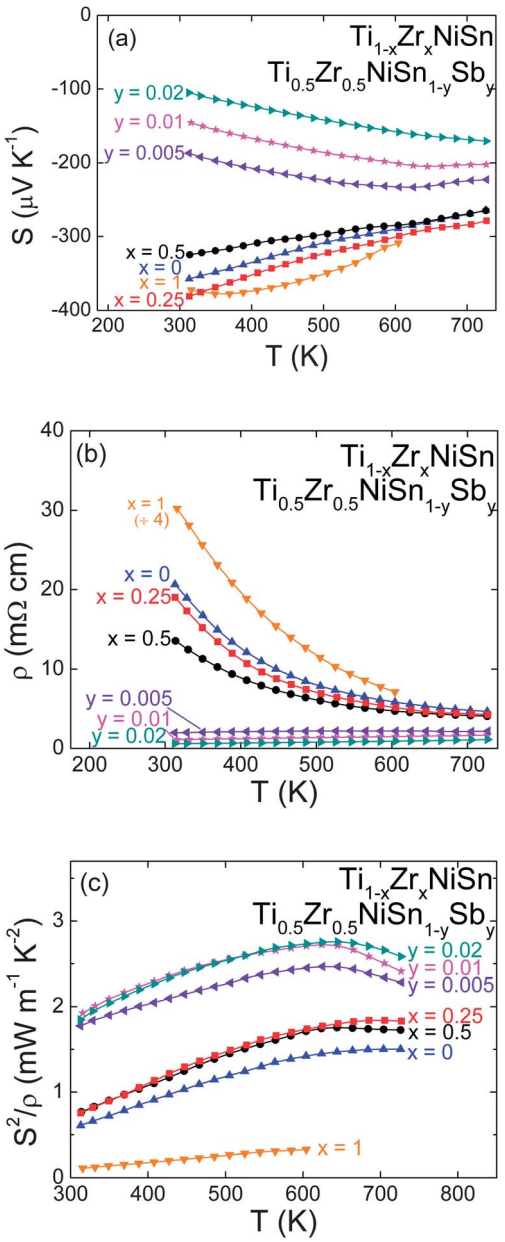

Fig. 3 Temperature dependence of (a) the Seebeck coefficient (S), (b) the electrical resistivity (ρ) and (c) the power factor (S^2/ρ) for the $Ti_{1-x}Zr_xNiSn$ and $Ti_{0.5}Zr_{0.5}NiSn_{1-y}Sb_y$ series.

Table 2 Densities, room temperature Seebeck (S) and resistivity (ρ) values and maximum power factor (S^2/ρ) for $Ti_{1-x}Zr_xNiSn_{1-y}Sb_y$, $Zr_{1-x}Hf_xNiSn$ and $Ti_{1-x}Hf_xNiSn$

Composition	Density (% of theoretical)	S (μV K^{-1})	ρ (mΩ cm)	Max. S^2/ρ (mW m^{-1} K^{-1})
TiNiSn	77	−357	20.6	1.5 (700 K)
$Ti_{0.75}Zr_{0.25}NiSn$	83	−381	19.0	1.8 (700 K)
$Ti_{0.5}Zr_{0.5}NiSn$	80	−324	13.6	1.8 (645 K)
$Ti_{0.25}Zr_{0.75}NiSn$	81	−225	12.1	1.4 (685 K)
ZrNiSn	68	−372	121.6	0.3 (605 K)
$Ti_{0.5}Zr_{0.5}NiSn_{0.99}Sb_{0.01}$	81	−145	1.1	2.7 (625 K)
$Ti_{0.5}Zr_{0.5}NiSn_{0.98}Sb_{0.02}$	79	−105	0.6	2.8 (650 K)
HfNiSn	73	−237	19.1	0.8 (610 K)
$Zr_{0.5}Hf_{0.5}NiSn$	78	−301	20.3	1.6 (625 K)
$Ti_{0.5}Hf_{0.5}NiSn$	72	−314	19.1	1.4 (725 K)

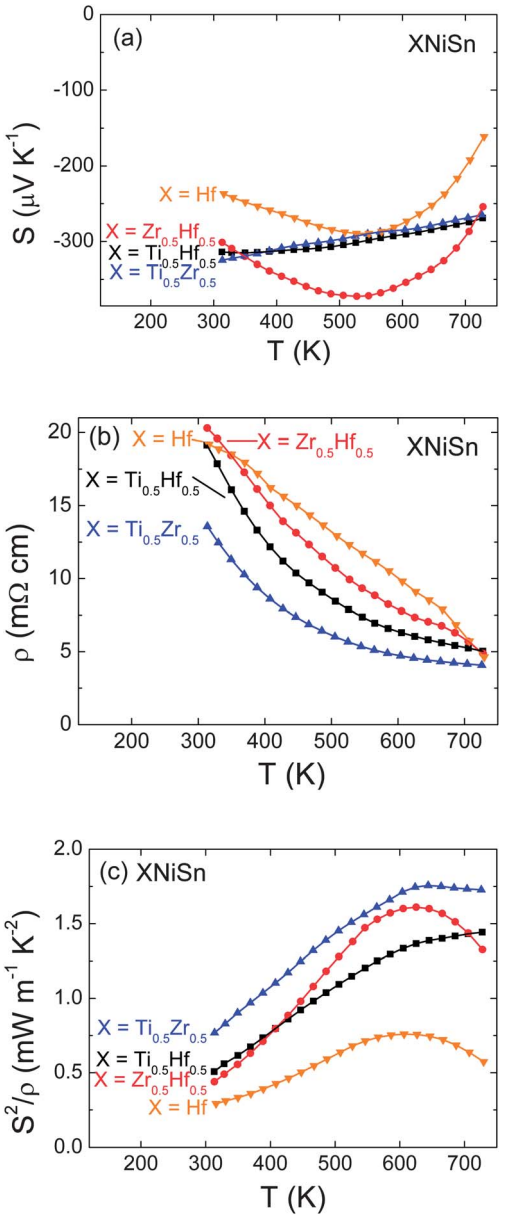

Fig. 4 Temperature dependence of (a) the Seebeck coefficient (S), (b) the electrical resistivity (ρ) and (c) the power (S^2/ρ) for the other studied XNiSn compositions (X = Hf, $Ti_{0.5}Zr_{0.5}$, $Ti_{0.5}Hf_{0.5}$ and $Zr_{0.5}Hf_{0.5}$).

Discussion

Structural analysis and elemental mapping of $X_{1-x}X'_xNiSn$ samples (with X and X′ chosen from Ti, Zr and Hf) has demonstrated that these materials exhibit multiphase behaviour for $x \neq 0,1$. In the case of $Ti_{0.5}Zr_{0.5}NiSn$ and $Ti_{0.5}Hf_{0.5}NiSn$ an almost continuous distribution of x-values exists, spanning a large x-interval ($\Delta x \leq 0.5$ and $\Delta x \leq 0.3$, respectively). For $Zr_{0.5}Hf_{0.5}NiSn$, narrower distributions centred around x_i values that span a similar interval are observed. The absence of a solid solution or two well-defined compositions of varying weight fractions precludes these systems from being under thermodynamic control. The end-members easily form phase pure materials (phase pure samples are obtained after only one day) and the multiphase behaviour must therefore be linked to the mixing of X–metals. However, the degree of multiphase behaviour does not simply scale with the size difference between Ti, Zr and Hf. This is evident from the difference in behaviour for the Ti–Zr and Ti–Hf series where a similar size difference between the X-cations exists. [An estimate of the size difference can be obtained from the lattice parameters; $a = 5.93$ Å (Ti); $a = 6.11$ Å (Zr) and $a = 6.08$ Å (Hf)]. It is also inconsistent with the similar spread in x_i values for the Zr–Hf series despite the small size difference. The electron microscopy clearly demonstrates that the compositional variations occur on multiple length scales, from 100 nm-scaled variations within some particles, through particle-by-particle structural variations on the micron scale and, indeed, with the suggestion that the scale of variations exceeds that of the FIB lamella. The observed $S(T)$ and ρ(T) values for the prepared series are in keeping with the wider literature on these materials, and in particular the $S(T)$ values for the $Ti_{1-x}Zr_xNiSn$ series are among the highest observed.[14]

The time dependent study undertaken on the $Ti_{0.5}Zr_{0.5}NiSn_{0.95}$ composition affords important insight into the distribution of phases in these samples (Fig. 5). After one day the elemental precursors have formed a ZrNiSn phase with sharp peaks and a broader hump corresponding to the mixed $Ti_{1-x}Zr_xNiSn$ phases. Upon annealing, these phases react and the $Ti_{1-x}Zr_xNiSn$ phases increase in abundance, gradually gaining a narrower distribution. The quantitative phase analysis (Fig. 5b) reveals that x_i and Δx_i (given as the error bars on the x_i values) do not change significantly after two weeks, which can also be seen directly from the peak shape (Fig. 5a). The system therefore never reaches equilibrium, and remains multiphase. Note that these samples were only mechanically homogenised once, after one day of annealing, after which it became impossible to cold-press pellets. The impact on the thermoelectric properties can be assessed by comparing $S(T)$, $\rho(T)$ and $\kappa(T) = \kappa_{lat}(T) + \kappa_{el}(T)$ for the samples annealed for 3 days (3 d) and 6 weeks (6 wk). The $\rho(T)$ and $S(T)$ are nearly identical for the 3 d and 6 wk samples demonstrating that the narrowing of the phase-distribution has little impact on the electronic properties (Fig. 5c and d). The anomaly in $\rho(T)$ at 500 K coincides with the melting point of Sn which is present as a minor impurity in the Sn deficient samples. Interpretation of $\kappa(T)$ is not straightforward as the raw data are affected by porosity effects due to the ~80% sample densities. Voids have a low κ and this can dominate the thermal response making it difficult to detect changes intrinsic to the material. The measured $\kappa(T)$ is identical for the 3 d and 6 wk samples and independent of temperature with an average $\kappa = 2.5$ W m^{-1} K^{-1}. This is a rather low value compared to the literature, suggesting porosity effects need to be taken into account. For this reason, the $\kappa(T) = \kappa_{lat}(T) + \kappa_{el}(T)$ data were normalized to the $\kappa(T)$ data for a >95% dense arc-melted $Ti_{0.5}Zr_{0.5}NiSn_{0.95}$ sample previously published.[18] The phase-distribution for this sample is given in Table S1.† The arc-melted sample has a temperature independent $\kappa(T)$ between 350 and 700 K with an average $\kappa = 4.3$ W m^{-1} K^{-1}. This yields a scaling factor (~1.7) that was applied to $\kappa_{lat}(T) = \kappa(T) - \kappa_{el}(T)$ for the 3 d and 6 wk samples, where $\kappa_{el}(T) = LT/\rho(T)$ was calculated using the $\rho(T)$ data in Fig. 5c ($L = 2.4 \times 10^{-8}$ W Ω K^{-2}). The

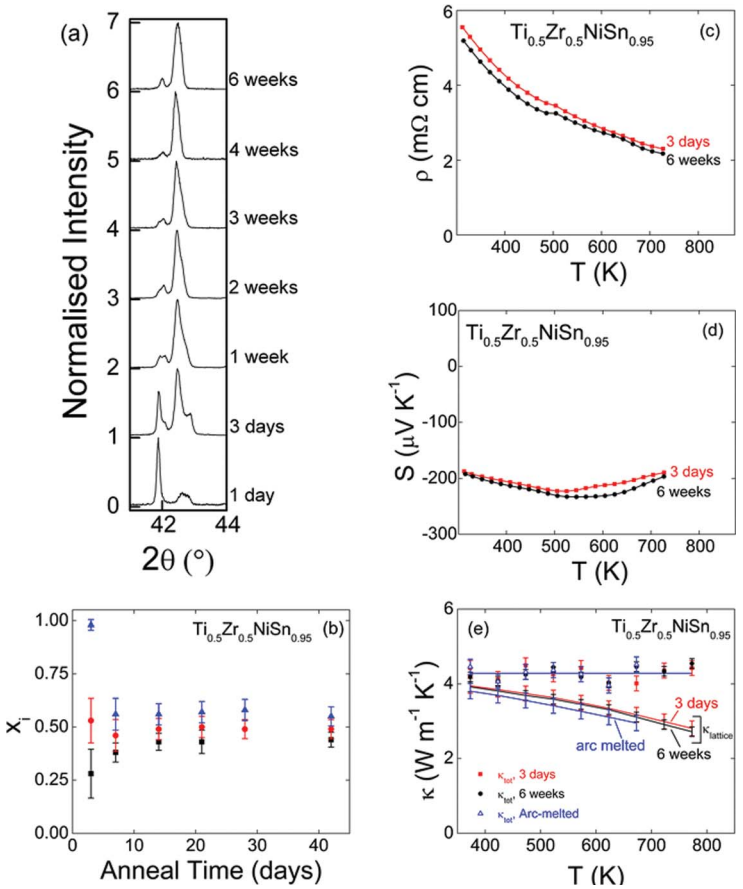

Fig. 5 Evolution of the compositional distribution and thermoelectric properties of $Ti_{0.5}Zr_{0.5}NiSn_{0.95}$ as a function of annealing time. Part (a) shows a close up to the (422) reflection. Part (b) shows the evolution of x_i and Δx_i (represented by the error bars) for phases with a >10 wt% abundance. Parts (c), (d) and (e) show the temperature dependence of the resistivity (ρ), the Seebeck coefficient (S) and the normalised (κ) and lattice (κ_{lat}) thermal conductivities (see manuscript text for details of the normalisation), for samples annealed for 3 days (red squares) and 6 weeks (black circles).

normalised $\kappa(T)$ and $\kappa_{lat}(T)$ for the 3 d, 6 wk and arc-melted samples are given in Fig. 5e. It is clear that the three samples have an identical $\kappa_{lat}(T)$, despite differences in annealing and preparation method. This suggests that the main reduction in κ_{lat} results from Ti/Zr mass and size difference phonon scattering with the multiphase behaviour a secondary contribution. The $\rho(T)$ data provide further justification for the porosity correction. The corrected ρ-values for the 3 d and 6 wk samples are 3.2 mΩ cm at 300 K and 1.3 mΩ cm at 700 K, which compares favourably with $\rho(T)$ for the arc-melted sample that has a similar semiconducting temperature dependence with $\rho_{300K} = 2$ mΩ cm and $\rho_{700K} = 1.2$ mΩ cm.[18] The $S(T)$ data for the 3 d and 6 wk samples are not affected by porosity and show a maximum of -230 μV K^{-1} at 550 K above which minority carriers reduce $S(T)$. The $S(T)$ of the arc-melted sample gradually increases from $S_{300K} = -130$ μV K^{-1} to $S_{700K} = -190$ μV K^{-1}.[18] The larger $S(T)$ and the presence of a maximum suggest that the present samples have a lower charge carrier concentration. The resulting maximum power factors are similar with $S^2/\rho \sim 3.5$ mW m^{-1} K^{-1} for the 3 d, 6 wk samples (650 K) and $S^2/\rho = 3$ mW m^{-1} K^{-1} for the arc-melted sample (700 K).

The $\rho(T)$ and S(T) data for $Ti_{1-x}Zr_xNiSn_{0.95/1.00}$, $Ti_{1-x}Hf_xNiSn$, $Zr_{1-x}Hf_xNiSn$ and the time dependent study in Fig. 5 suggest that the multiphase behaviour has a modest impact on the electronic properties. This is evidenced by the similar $S(T)$ and $\rho(T)$ and the improved S^2/ρ values for the mixed phase samples compared to the single phase end-members (Fig. 3, 4, S3,† and Table 2). This observation is also consistent with X-ray diffraction and electron microscopy, which taken together, suggest that the major compositional variations occur over length scales that exceed the FIB lamella. In this situation, the multiphase length scales are greater than typical electron mean free paths, and only a small impact on $\rho(T)$ and $S(T)$ is expected. Assessing the impact on $\kappa_{lat}(T)$ is much more difficult due to the larger range of length scales involved.[25] The data for $Ti_{0.5}Zr_{0.5}NiSn_{0.95}$ suggests that the dominant reduction from $\kappa \approx 10$ W m^{-1} K^{-1} for the end-members (ref. 26) to $\kappa \approx 4$ W m^{-1} K^{-1} is related to Ti/Zr mass and size difference scattering of phonons with the multiphase behaviour making a smaller contribution. The high ZT materials reported in the literature contain mixtures of Ti, Zr and Hf and have $\kappa_{lat} = 2$–3 W m^{-1} K^{-1}. This further reduction could be linked to a multiphase contribution as the nature of the interfaces will depend on composition and sample processing.[14,16,17] Additional experiments are needed to assess the specific impact of the multiphase behaviour on the thermal conductivity in the wider family of XNiSn materials. There is

great current interest in nanostructured half-Heuslers with formula $XNi_{1+y}Sn$.[18,24,27–32] In these materials, the excess Ni (y) is present as interstitials and as full-Heusler (nano) precipitates (*e.g.* $TiNi_2Sn$). The electron microscopy data reported here do not show any evidence for the presence of nano-inclusions, which is as expected, in keeping with the stoichiometric starting compositions. The diffraction data suggest the presence of some interstitial Ni in the Sn deficient materials (*e.g.* $TiNiSn_{0.95} \rightarrow TiNi_{1.01}Sn$). This may have an impact on the thermoelectric properties, and in particular on κ_{lat}, although the amount is small compared to reports where significant reductions of κ_{lat} were observed ($y = 0.05 - 0.2$).[18,24,28]

To summarize, the key conclusion from our quantitative diffraction and microscopy study is that all XNiSn half-Heuslers (where X is a mixture of Ti, Zr and Hf) exhibit multiphase behaviour due to kinetic limitations during the synthesis. The main compositional variations occur over length scales greater than the FIB lamella (2.5×4.5 μm^2) with smaller particle by particle and variations within particles also evident. The similar $\rho(T)$ and $S(T)$ and improved S^2/ρ values demonstrate that the multiphase behaviour is not detrimental to the electronic transport, while further work is needed to assess the precise impact on the thermal conductivity of the XNiSn compositions.

Acknowledgements

We acknowledge support from the EPSRC (EP/J000884/1) and the Royal Society.

References

1 G. J. Snyder and E. S. Toberer, *Nat. Mater.*, 2008, **7**, 105–114.
2 J. R. Sootsman, D. Y. Chung and M. G. Kanatzidis, *Angew. Chem., Int. Ed.*, 2009, **48**, 8616–8639.
3 G. S. Nolas, J. Poon and M. Kanatzidis, *MRS Bull.*, 2006, **31**, 199–205.
4 A. J. Minnich, M. S. Dresselhaus, Z. F. Ren and G. Chen, *Energy Environ. Sci.*, 2009, **2**, 466–479.
5 M. G. Kanatzidis, *Chem. Mater.*, 2010, **22**, 648–659.
6 C. J. Vineis, A. Shakouri, A. Majumdar and M. G. Kanatzidis, *Adv. Mater.*, 2010, **22**, 3970–3980.
7 M. Zebarjadi, K. Esfarjani, M. S. Dresselhaus, Z. F. Ren and G. Chen, *Energy Environ. Sci.*, 2012, **5**, 5147–5162.
8 H. C. Kandpal, C. Felser and R. Seshadri, *J. Phys. D: Appl. Phys.*, 2006, **39**, 776–785.
9 T. Graf, C. Felser and S. S. P. Parkin, *Prog. Solid State Chem.*, 2011, **39**, 1–50.
10 C. Uher, J. Yang, S. Hu, D. T. Morelli and G. P. Meisner, *Phys. Rev. B: Condens. Matter Mater. Phys.*, 1999, **59**, 8615–8621.
11 Y. Xia, S. Bhattacharya, V. Ponnambalam, A. L. Pope, S. J. Poon and T. M. Tritt, *J. Appl. Phys.*, 2000, **88**, 1952–1955.
12 S. Bhattacharya, A. L. Pope, R. T. Littleton, T. M. Tritt, V. Ponnambalam, Y. Xia and S. J. Poon, *Appl. Phys. Lett.*, 2000, **77**, 2476–2478.
13 Q. Shen, L. Chen, T. Goto, T. Hirai, J. Yang, G. P. Meisner and C. Uher, *Appl. Phys. Lett.*, 2001, **79**, 4165–4167.
14 S. Sakurada and N. Shutoh, *Appl. Phys. Lett.*, 2005, **86**, 082105.
15 S. R. Culp, S. J. Poon, N. Hickman, T. M. Tritt and J. Blumm, *Appl. Phys. Lett.*, 2006, **88**, 042106.
16 M. Schwall and B. Balke, *Phys. Chem. Chem. Phys.*, 2013, **15**, 1868–1872.
17 S. Populoh, M. H. Aguirre, O. C. Brunko, K. Galazka, Y. Lu and A. Weidenkaff, *Scr. Mater.*, 2012, **66**, 1073–1076.
18 R. A. Downie, D. A. MacLaren, R. I. Smith and J. W. G. Bos, *Chem. Commun.*, 2013, **49**, 4184–4186.
19 Y. Gelbstein, N. Tal, A. Yarmek, Y. Rosenberg, M. P. Dariel, S. Ouardi, B. Balke, C. Felser and M. Kohne, *J. Mater. Res.*, 2011, **26**, 1919–1924.
20 T. Katayama, S. W. Kim, Y. Kimura and Y. Mishima, *J. Electron. Mater.*, 2003, **32**, 1160–1165.
21 A. C. Larson and R. B. Von Dreele, in *General Structure Analysis System (GSAS)*, 2000.
22 B. H. Toby, *J. Appl. Crystallogr.*, 2001, **34**, 210–213.
23 D. B. Willams and C. B. Carter, *Transmission Electron Microscopy*, Springer, New York, 1996.
24 Y. W. Chai and Y. Kimura, *Acta Mater.*, 2013, **61**, 6684–6697.
25 J. Shiomi, K. Esfarjani and G. Chen, *Phys. Rev. B: Condens. Matter Mater. Phys.*, 2011, **84**, 104302.
26 H. Hohl, A. P. Ramirez, W. Kaefer, K. Fess, C. Thurner, C. Kloc and E. Bucher, in *Thermoelectric Materials – New Directions and Approaches*, eds. T. M. Tritt, M. G. Kanatzidis, H. B. Lyon and G. D. Maham, 1997, pp. 109–114.
27 C. S. Birkel, J. E. Douglas, B. R. Lettiere, G. Seward, N. Verma, Y. C. Zhang, T. M. Pollock, R. Seshadri and G. D. Stucky, *Phys. Chem. Chem. Phys.*, 2013, **15**, 6990–6997.
28 Y. W. Chai and Y. Kimura, *Appl. Phys. Lett.*, 2012, **100**, 033114–033113.
29 J. E. Douglas, C. S. Birkel, M. S. Miao, C. J. Torbet, G. D. Stucky, T. M. Pollock and R. Seshadri, *Appl. Phys. Lett.*, 2012, **101**, 183902.
30 H. Hazama, M. Matsubara, R. Asahi and T. Takeuchi, *J. Appl. Phys.*, 2011, **110**, 063710–063716.
31 J. P. A. Makongo, D. K. Misra, X. Zhou, A. Pant, M. R. Shabetai, X. Su, C. Uher, K. L. Stokes and P. F. P. Poudeu, *J. Am. Chem. Soc.*, 2011, **133**, 18843–18852.
32 J. P. A. Makongo, D. K. Misra, J. R. Salvador, N. J. Takas, G. Wang, M. R. Shabetai, A. Pant, P. Paudel, C. Uher, K. L. Stokes and P. F. P. Poudeu, *J. Solid State Chem.*, 2011, **184**, 2948–2960.

